

Received: 7 March 2021

Revised: 24 March 2021

Accepted: 25 March 2021

# Wearable microneedle dual electrochemical sensor for simultaneous pH and cortisol detection in sweat

Samuel M. Mugo<sup>1</sup> | Weihao Lu<sup>1</sup> | Marika Wood<sup>1</sup> | Stephane Lemieux<sup>2</sup>

<sup>1</sup> Physical Sciences Department,  
 MacEwan University, Edmonton, Canada

<sup>2</sup> Department of Decision Sciences,  
 MacEwan University, Edmonton, Canada

## Correspondence

Samuel M. Mugo, Physical Sciences  
 Department, MacEwan University,  
 Edmonton, Canada.

Email: [mugos@macewan.ca](mailto:mugos@macewan.ca)

## Abstract

We report herewith an inexpensive flexible dual target electrochemical sensor for simultaneous detection of pH and cortisol in human sweat. The sensor was fabricated by printing layer by layer (LbL) on a conductive microneedle polydimethylsiloxane (PDMS) flexible substrate. The dual sensor integrates two detection chambers comprising polyaniline (PANI) and cortisol imprinted poly (glycidylmethacrylate-co ethylene glycol dimethacrylate) (poly (GMA-co-EGDMA)). The dual wearable sensor rapidly (< 1 min) responded linearly to pH in the range of 3–9, while the cortisol sensor chamber had a linear range of 0–100 ng/mL. The cortisol sensing region had an excellent limit of detection (LOD) of  $1.4 \pm 0.3$  ng/mL, with intra-batch reproducibility of 2.4% relative standard deviation (%RSD). The inter-batch precision (%RSD for three different sensors) was determined to be 4.7%. Demonstrating excellent stability and reusability, a single patch of cortisol sensor was used for 15 times over a 30-day period, with minimal change in response. The dual analyte wearable sensors were effective for detection of pH and cortisol in real human sweat.

## KEYWORDS

capacitive sweat sensors, dual electrochemical sensor for simultaneous pH and cortisol detection, microneedle biomimetic flexible e-skin sensors, PANI-based pH sensors, poly (GMA-co-EDMA) cortisol imprinted polymer film

## 1 | INTRODUCTION

Wearable sensor analytics platforms, also referred to as e-skins, are revolutionary and rapidly growing in real-time monitoring and diagnostics in key demand areas such as precision agriculture, precision medicine, health awareness, and personalized therapy.<sup>[1,2]</sup> Compared to traditional chemical analysis techniques, wearable sensors have the superiority of low cost, user-friendliness, portability, and point of care real-time monitoring. With significant growth in the accompanying software embedded

analytics, wearable sensors can provide individuals with the real-time data necessary for proactive decision-making on their health and wellness.<sup>[1]</sup> The conventional disease diagnosis approach requires monitoring biochemical metabolites present in biological fluids such as blood and urine, which are invasive and not ideal for real-time analysis. Sweat is a desirable alternative biofluid for real-time monitoring. Similar to the kidney and lungs, sweat glands act as the excretory organ for drugs and metabolites.<sup>[3]</sup> Sweat contains multiple chemical biomarkers that alter its pH. Based on pH partition theory, human sweat is

This is an open access article under the terms of the [Creative Commons Attribution](https://creativecommons.org/licenses/by/4.0/) License, which permits use, distribution and reproduction in any medium, provided the original work is properly cited.

© 2021 The Authors. *Electrochemical Science Advances* published by Wiley-VCH GmbH

more acidic than blood with a pH range from 4.5 to 7.0<sup>[4,5]</sup> due to factors such as drug accumulation and the presence of metabolic by-products such as urea, lactate, and bicarbonate.<sup>[3,6,7]</sup> Patients with cystic fibrosis have alkaline sweat (up to pH 9) due to ineffective bicarbonate-reabsorption. As such, the pH level in sweat is a key physiological indicator that can provide diagnostic information about skin diseases and associated skin microbiome, monitor wound healing processes, and muscle stress levels.<sup>[8]</sup> In addition, the sweat pH value is a sports performance indicator for intensity and dehydration levels.<sup>[5]</sup>

Sweat also contains specific metabolites such as cortisol, which can reveal important information about the mental health and wellbeing of an individual. The presence of cortisol in human sweat can be an indicator of vital physiological processes such as energy metabolism, electrolytic balance, and blood pressure, all of which influence cognitive processes such as working memory, sleep patterns, and mood.<sup>[9]</sup> Thus, cortisol can be a useful biomarker for diagnosing physiological conditions related to anxiety, depression, and mental health.<sup>[10]</sup> Simultaneous detection of pH and cortisol in real-time can help monitor the physiological status of the human body. With the growth of the mental health pandemic, wearable cortisol sensors that monitor the real-time fluctuations of human emotions and inherent triggers could improve the general public's health and wellness outcomes, especially in vulnerable groups such as individuals with autism and social disorders. Additionally, the use of real-time cortisol sensing devices, especially among young learners with autism, could be essential in understanding the triggers that impair their learning.<sup>[11–16]</sup>

While most e-skin sensors are developed to rest on the skin surface, a microneedle-based e-skin platform may be preferred as it would allow for the effective monitoring of metabolites in the interstitial fluids rather than just sweat. The emerging medical analysis of interstitial fluid is desirable as it is more diagnostically relevant than sweat. Interstitial fluid contains many of the same metabolites as blood, while sampling remains less invasive.<sup>[17–20]</sup> However, development of flexible microneedle wearable electronics remains a nascent field.<sup>[21]</sup> Microneedles, typically less than 1000  $\mu\text{m}$  in length, painlessly penetrate the membranous stratum corneum and increase the touching surface area for better sweat and interstitial fluid collection.<sup>[22]</sup>

In this article, we demonstrate a flexible microneedle dual responsive sensor comprising a polyaniline (PANi) pH responsive and a cortisol molecularly imprinted polymer (MIP) biomimetic receptor chambers, printed side by side. The PANi layer pH-responsive chamber addresses the limitations of the conventional glass pH electrode, which is impractical for fashioning into wearable devices. Due to its pH-dependent emeraldine salt-emeraldine base

transition, the PANi offers outstanding pH sensing properties in aqueous media.<sup>[23,24]</sup> Furthermore, the cortisol MIP based on poly(glycidylmethacrylate-co ethylene glycol dimethacrylate)(poly(GMA-co-EGDMA)) has been verified to have high affinity and fast-response to cortisol.<sup>[9,14]</sup> The MIP technique is a more versatile approach to make cortisol biomimetic receptors compared to the traditional antibody/or enzyme-linked immunosorbent assays, which tend to be laborious, expensive, and environmentally unstable.<sup>[25–27]</sup>

The reported dual pH and cortisol wearable sensor is based on a layer-by-layer (LbL) printing of the sensor's polymer biomimetic recognition element, namely PANi and cortisol imprinted poly (GMA-co-EGDMA) on a conductive microneedle polydimethylsiloxane (PDMS) substrate. The dual sensor is  $1.5 \times 3.0$  cm in size and  $\sim 1$ – $2$  mm thickness, with screen printed counter and reference electrodes integrated onto the sensor platform. Based on the materials used for fabrication, the pH and cortisol sensors are labeled PDMS@CNC/CNT/PDMS@PANi and PDMS@CNC/CNT/PDMS@PANi@MIP, respectively.

## 2 | EXPERIMENTAL SECTION

### 2.1 | Materials and methods

The carboxylic acid functionalized multi-walled CNTs (OD: 4–6 nm. 98% pure) was purchased from Times-Nano, China. Potassium ferricyanide ( $\text{K}_3[\text{Fe}(\text{CN})_6]$ ), 3-glycidyloxypropyl trimethoxysilane (GOPS), ammonium peroxydisulfate (APS), toluene, 4,4'-azobis(4-cyanovaleric acid) (ACVA), naphthalene, hydrocortisone, glycidylmethacrylate (GMA), ethylene glycol dimethacrylate (EGDMA), and cyclohexanol were procured from Sigma-Aldrich, Ontario, Canada. Aniline was bought from Fisher Scientific, USA. Cellulose nanocrystals (CNC) were donated by Alberta Innovates. The Dow and Corning's Sylgard 184, polydimethylsiloxane (PDMS) was purchased from Dow Corning Corporation, Midland, Michigan, United States. The Ecoflex 00–30 part A and part B was bought from Smooth-on Incorporation, Edmonton, Alberta, Canada. All other reagents were of analytical reagent grade. All aqueous solutions were prepared using  $> 18$  MW Milli-Q deionized (DI) water.

### 2.2 | Fabrication of the flexible microneedle sensor patch

To fabricate the microneedle PDMS patch, 15 g of beeswax was melted on a hot plate ( $75^\circ\text{C}$ ) in a glass container ( $10.0 \times 15.0 \times 6.5$  cm) and allowed to solidify through

cooling to room temperature. A female microneedle template was printed on the beeswax mold by stamping with a microneedle roller (M.T. brand, model MT2.5, needle dimension 0.25 mm). A 20 g PDMS prepolymer mixture comprising: 45% Sylgard 184 PDMS silicone base, 5% silicone curing agent, 25% EcoFlex 00–30 Part A, and 25% EcoFlex 00–30 Part B, was poured into the female microneedle wax mold and cured at room temperature for a week. The male microneedle PDMS patch was then removed from the beeswax mold, resulting in PDMS microneedles with a length of  $\sim 250$   $\mu\text{m}$ . The microneedle PDMS patches were cut into  $1 \times 1.5$  cm segments, with 110 microneedles per patch. The microneedle PDMS patch was then evenly coated by spreading a thin layer of 0.15 g of conductive PDMS@CNC/CNT gel (composition delineated *vide infra*) using a glass rod, followed by overnight curing at  $80^\circ\text{C}$ . The conductive PDMS@CNC/CNT gel printed on the microneedle PDMS patch was prepared by mixing 0.2 g multiwalled CNTs, 0.2 g CNC, 7 mL of toluene, 800  $\mu\text{L}$  of 1000 ppm naphthalene dissolved in acetonitrile, 1.9 g Sylgard 184 PDMS base, and 0.2 g silicone curing agent. To ensure complete homogeneity of the suspension, CNT and CNC was first suspended in toluene and naphthalene and sonicated for 1 h. Subsequently, 1.9 g of Sylgard 184 PDMS silicone base was added to the homogeneous CNT/CNT suspension and sonicated for 1 h. The suspension was stirred using a stir plate at  $50^\circ\text{C}$  for 24 h to evaporate all toluene. Finally, 0.2 g of Sylgard 184 PDMS curing agent was added to the suspension and thoroughly mixed with a glass stirring rod, resulting in a highly viscous and homogeneous conductive gel.

### 2.3 | Integration of the pH-responsive PANi layer to the microneedle PDMS@CNC/CNT patch

To integrate the pH responsive layer to the microneedle PDMS@CNC/CNT patch, a PANi layer was employed. The PANi prepolymer mixture comprised 0.2 M aniline, 1 mg/ml CNT, 4 mg/mL CNC, and 1 M  $\text{H}_2\text{SO}_4$ . The mixture was prepared by first adding 12 mg CNC to 2.3 mL DI water and stirring overnight, followed by adding 3 mg CNT and sonicating the mixture for 6 h to create a homogeneous suspension. Subsequently, 0.6 mL of 5 M  $\text{H}_2\text{SO}_4$  and 54  $\mu\text{L}$  of aniline were added to the homogeneous CNC/CNT suspension. A 10  $\mu\text{L}$  PANi prepolymer mixture aliquot with 5  $\mu\text{L}$  of 1.5 M APS initiator was evenly spread on the microneedle PDMS@CNC/CNT patch and left to polymerize on an ice bath for 1 h. Following polymerization, the pH responsive PDMS@CNC/CNT/PDMS@PANi was left overnight in a dehydrator at room temperature to dry.

### 2.4 | Fabrication of microneedle PDMS@CNC/CNT/PDMS@PANi@MIP cortisol sensor patch

The cortisol imprinted layer was printed on the microneedle PDMS@CNC/CNT/PDMS@PANi patch by adapting the prepolymer system reported by Mugo et al.<sup>[9]</sup> The cortisol imprinted prepolymer mixture comprised 400  $\mu\text{L}$  cyclohexanol, 26  $\mu\text{L}$  GMA, 80  $\mu\text{L}$  EGDMA, 2.0 mg ACVA, and 1.5 M cortisol dissolved in a 1:1 (v/v) mixture of water and acetonitrile. A 30  $\mu\text{L}$  aliquot of the cortisol prepolymer mixture was evenly spread and subsequently polymerized on the microneedle PDMS@CNC/CNT/PDMS@PANi patch at  $70^\circ\text{C}$  oven for 4 h. The non-imprinted polymer (NIP) control sensor was polymerized in the same manner, but the prepolymer was free of the cortisol template. Following polymerization, the cortisol template was removed using cyclic voltammetry (CV) electrochemical cleaning method reported in previous work.<sup>[9]</sup> The CV was acquired using PalmSens 4 potentiostat with PStTrace software (PalmSens BV, the Netherlands). The films were electrochemically cleaned by immersing them in 10 mL of 0.1 M phosphate buffer (pH 7.0) in a conventional electrochemical cell, with commercial Ag/AgCl reference electrode, and platinum wire counter electrode. Five CV cycles were conducted to ensure all the cortisol had been washed out. The CV was acquired with potentials in the range of  $-0.9$  to  $+0.9$  V using a scan rate of 0.1 V/s. After each wash cycle, the phosphate buffer was changed, and five more CV cycles were conducted. Three washing cycles were performed for a total of 15 CV cycles.

### 2.5 | Assembly of the pH and cortisol microneedle sensors

The pH and cortisol microneedle patches were glued to a polyvinylacetate (PVA) transparency as a substrate. To make the inhouse printed reference electrode, 10 mg silver nanoparticles (AgNP) were bleached overnight with 2 mL of Clorox® Bleach and allowed to air dry, followed by resuspension in 1 mL of CNT/CNC (1 mg/mL / 4 mg/mL). A PVA transparency sheet ( $0.3 \times 2.0$  cm) was then evenly coated with 200  $\mu\text{L}$  bleached AgNP/CNT/CNC composite suspension and allowed to air dry at room temperature. The auxiliary electrode was similarly prepared by coating the PVA transparency strip with 200  $\mu\text{L}$  of CNT/CNC (1 mg/mL/4 mg/mL) and allowed to air dry at room temperature. The in-house reference and auxiliary electrodes were glued in proximity to the dual pH and cortisol microneedle patches. The schematic in Figure 1A shows a depiction of the resulting dual pH and cortisol

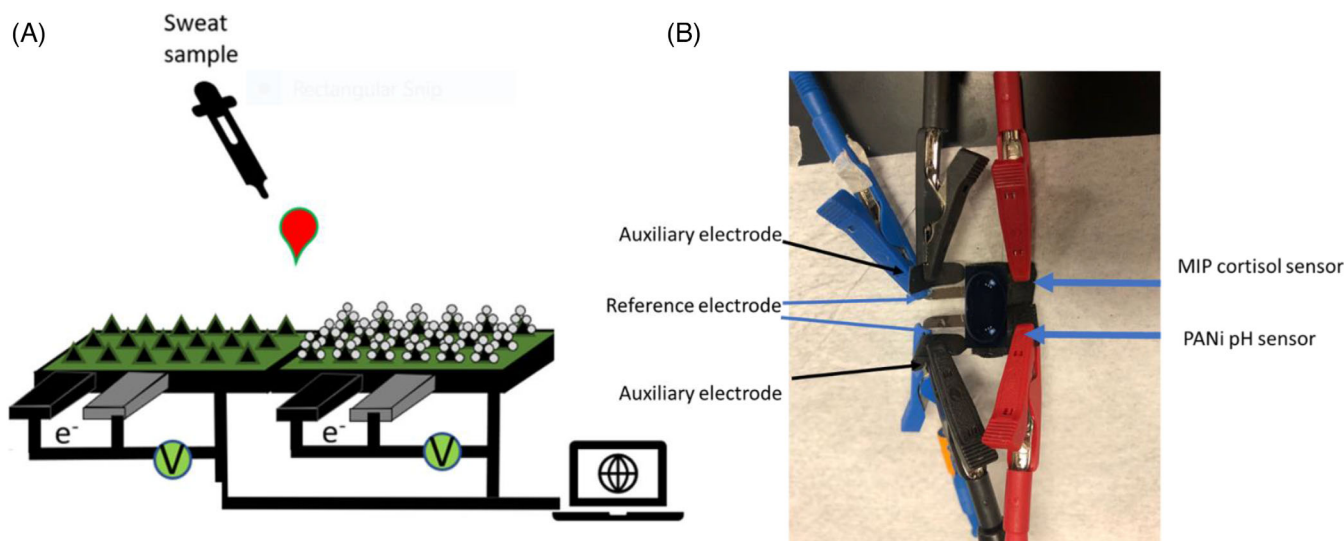


**FIGURE 1** (A) Schematic depicting the dual pH and cortisol MIP sensor patch; (B) Picture demonstrating the dual sensor electrochemical connections

microneedle sensors, while Figure 1B illustrates the sensor patches electrochemical connection.

## 2.6 | Characterization of the dual pH and cortisol imprinted microneedle sensors

Using a Palmsens 4 potentiostat with PSTrace software, the dual pH and cortisol microneedle sensors were characterized using electrochemical measurements including CV and electrochemical impedance spectroscopy (EIS) with 25 mM  $K_3FeCN_6$  in 0.1 M KCl as a standard redox probe. The Zeiss Sigma 300 VP field emission scanning electron micrograph (SEM) was used to characterize the morphology of the microneedle electrodes. The IR spectra were recorded on a Bruker Tensor 27 FTIR instrument fitted with diamond attenuated total reflectance (ATR).

## 2.7 | Testing of the pH and cortisol imprinted microneedle sensors

First, the PDMS@CNC/CNT@PANi pH sensor was tested for its response to changes in pH. In a beaker, a solution of 1 M NaOH was adjusted with 1 M HCl between a pH range of 3.0–9.3, with the change in pH validated with a commercial pH electrode. Using the pH patch sensor, cyclic voltammograms were acquired for the different pH solutions at a voltage range of  $-0.95$  to  $+0.95$  V and a scan rate of 0.10 V/s. Prior to taking the measurements, the pH patch sensor was immersed in the test solution for a 1 min equilibration time. The capacitance signal change as a function of pH change was determined from the

cyclic voltammograms by taking a ratio of current to scan rate.

The PDMS@CNC/CNT@PANi @MIP cortisol sensor was evaluated for its responsivity to cortisol standards at pH 7.0 and 4.5, prepared with 1 M NaOH and adjusted with 1 M HCl. Each solution with fixed pH was spiked with 30  $\mu$ L aliquot additions of 1500 ng/mL hydrocortisone dissolved in 0.1 M KCl. The experiment was repeated for both MIP and NIP cortisol sensor platforms.

## 2.8 | Real sweat analysis

The dual pH sensor and MIP cortisol sensor were further evaluated for the detection of pH and cortisol in a real sweat sample. The sweat sample was collected in a vial from the brow of a volunteer, following vigorous exercise. For analysis, the dual sensor was tested by adding a 1000  $\mu$ L aliquot of 0.1 M KCl blank solution and the background signal was acquired by CV. A 50  $\mu$ L of sweat sample aliquot was deposited onto the blank aliquot and analyzed, followed by nine sequential additions of 10  $\mu$ L of 1500 ng/mL of cortisol standard with CV acquired in triplicate after each addition. Before acquiring the CV, a 1 min residence time was allowed for molecular interactions between the MIP biomimetic receptors and the cortisol to ensue. A standard addition calibration was derived, and the pH and cortisol concentrations determined in the sweat sample. Further analysis of the dual pH and cortisol sensor was completed to test detection from sweat when used as a wearable device. The microneedle sensor patches were attached to the surface of the skin on the upper arm and secured using a tape. The participant underwent 30 mins

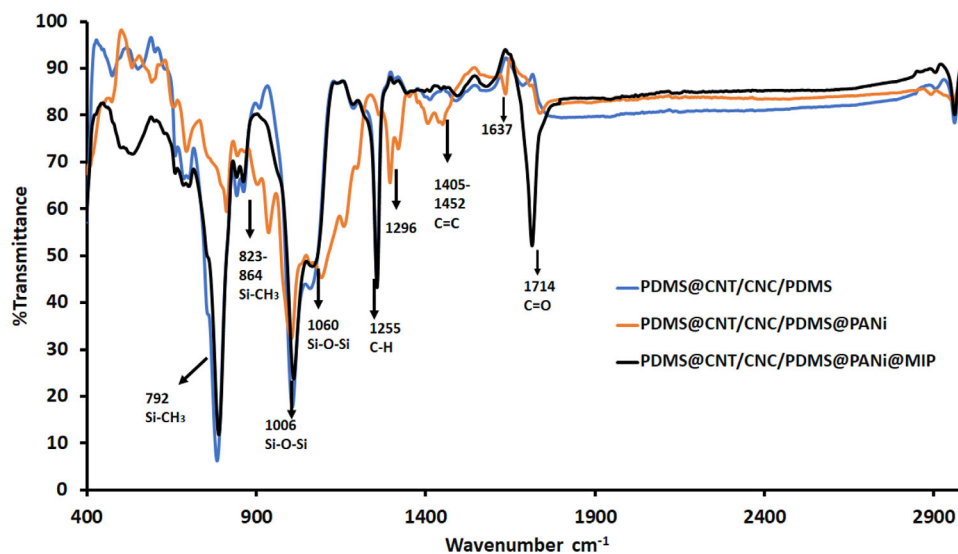


FIGURE 2 Overlapped FTIR spectra for PDMS@CNT/CNC/PDMS, PDMS@CNT/CNC/PDMS@PANI and PDMS@CNT/CNC/PDMS@PANI@MIP

of vigorous exercise to stimulate sweat generation, and the CV was obtained via Bluetooth using a wireless PalmSens potentiostat with PSTrace software and a computer tablet. The pH and cortisol amounts in the sweat were quantified using the previously generated external calibration method.

## 2.9 | Calibration curve and statistical models

The capacitance in the resulting cyclic voltammograms for both pH and cortisol sensors was averaged in the 0.25–0.50 V range and plotted as a function of change in concentrations resulting in linear calibration plots. To further develop robust linear calibrations, statistical analysis was applied to identify the voltages whose change in current best predict changes in pH and cortisol for the respective sensors. A correlation response matrix between current at variable voltages was prepared and a model based on the single best voltage predictor was selected. To produce candidate multilinear regression models, both forward and backward selection was employed and Least Absolute Shrinkage and Selection Operator (LASSO) regression for multiple lambda values.

The model selection was based on a balance between accuracy and simplicity, which was measured by adjusted R-square and either Akaike information criterion (AIC) or Bayesian information criterion (BIC), depending on the model, with AIC and BIC often coinciding. The model that best balanced the fewest predictors and lowest root mean squared error (RMSE) of the hold-out testing set was selected for each response variable. The voltage that

demonstrated the highest linear correlation to pH and cortisol were selected for the single linear model, with voltage distances restricted to multiples of 0.25 V used to reduce the possibility of multicollinearity and increase the reliability of the resulting models.

## 3 | RESULTS AND DISCUSSION

### 3.1 | Characterization of the dual pH and MIP cortisol wearable sensor

As evidence for the fabrication of each layer, the LbL sensor patches were characterized using FTIR, as shown by the overlapped spectra in Figure 2. All the patches had characteristic peaks including 792  $\text{cm}^{-1}$  attributed to Si-C stretching vibration, 864  $\text{cm}^{-1}$  related to Si-CH<sub>3</sub> rocking, 1006  $\text{cm}^{-1}$  related to Si-O-Si stretching vibrations and the broad bands around 530  $\text{cm}^{-1}$  assigned to Si-O-Si bending vibration.<sup>[28,29]</sup> These silicone-based peaks decreased with intensity with subsequent addition of the PANi and MIP layers.

The PDMS@CNT/CNC/PDMS@PANI had characteristic peaks at 1296–3121  $\text{cm}^{-1}$  and 1413–1454  $\text{cm}^{-1}$  assigned to the C-N stretching and C = C stretching vibrations of benzenoid and quinoid rings, indicative of PANi formation.<sup>[30]</sup> The addition of the cortisol imprinted poly (GMA-co-EGDMA) layer to the PDMS@CNT/CNC/PDMS@PANI patch showed a characteristic band at 1714  $\text{cm}^{-1}$  for C = O stretch.<sup>[31]</sup>

The morphology of the microneedle sensors were characterized using a SEM. Figure 3A shows the SEM image of the conductive PDMS@CNT/CNC/PDMS@PANI patches

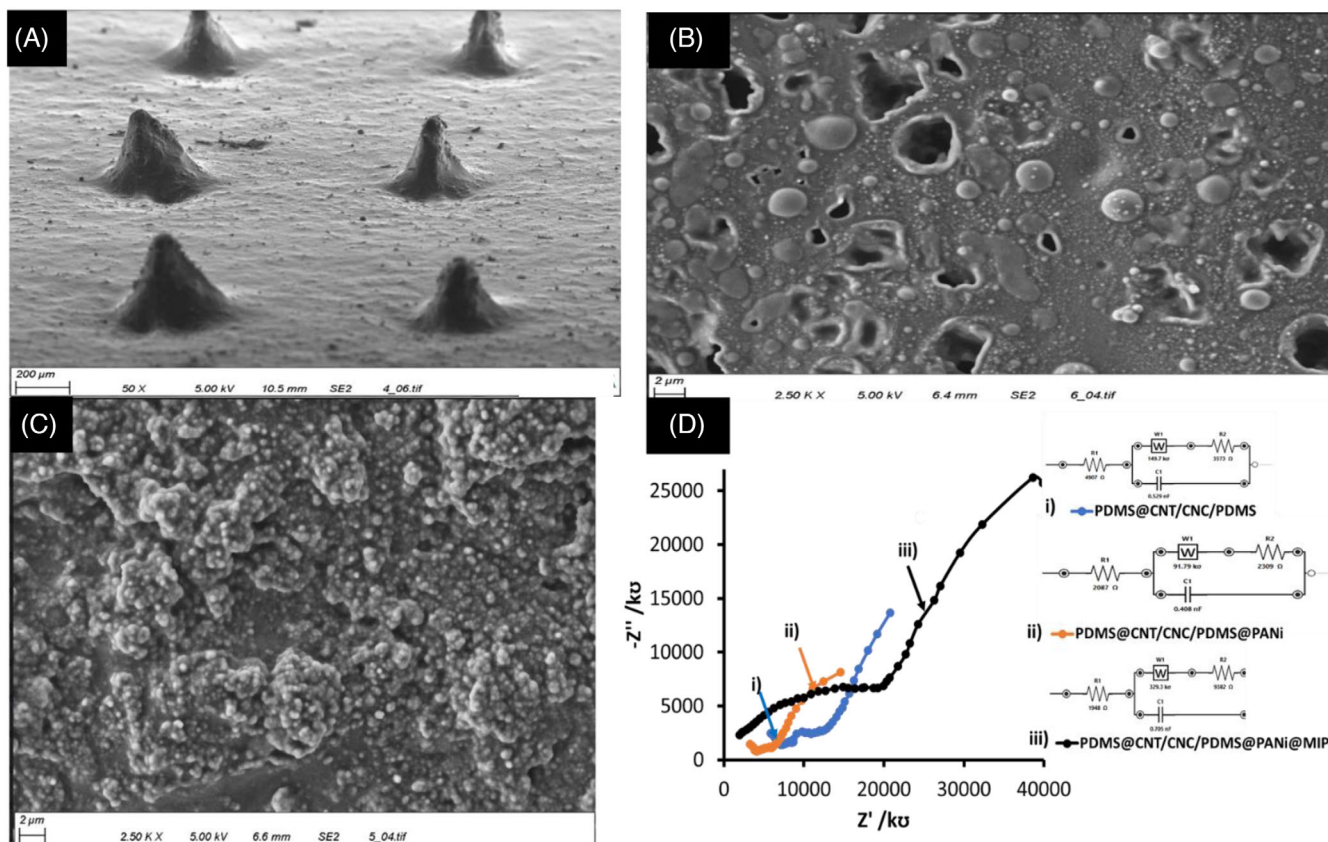


**FIGURE 3** Micrograph images of: (A) PDMS@CNT/CNC/PDMS@PANi patches; (B) electrochemically cleaned PDMS@CNT/CNC/PDMS@PANi@MIP patch; (C) PDMS@CNT/CNC/PDMS@PANi@NIP; (D) Nyquist plots of different microneedle sensor patches in 25 mM  $K_3FeCN_6$  dissolved in 0.1 M KCl

with well-defined  $\sim 300 \mu\text{m}$  tall microneedle structures with distances of  $\sim 650 \mu\text{m}$  between microneedles, resulting in 110 microneedle density for the  $1 \times 1.5 \text{ cm}$  patch. Figure 3B,C shows the surfaces of the electrochemically cleaned PDMS@CNT/CNC/PDMS@PANi@MIP and NIP sensor patches, respectively. The electrochemically cleaned cortisol MIP sensor patch image provides evidence of microcavities, which are arguably the cortisol receptors. Evident in Figure 3B, the porosity of the cortisol MIP sensor patches are varied with the cavities ranging from  $\sim 50 \text{ nm}$  to  $\sim 2 \mu\text{m}$ . However, the NIP platform does not have the same distinct microcavities as the MIP.

The dual pH and cortisol sensor patches were further characterized by electrochemical impedance spectroscopy (EIS). Figure 3D shows the Nyquist plots for PDMS@CNT/CNC, PDMS@CNT/CNC/PDMS@PANi, and PDMS@CNT/CNC/PDMS@PANi@MIP patches, respectively, analyzed using 25 mM  $K_3FeCN_6$  solution in 0.1 M KCl. The smaller the semicircle in the high-frequency region of the Nyquist plots, the smaller the value of the electron transfer resistance ( $R_{ct}$ ). The  $R_{ct}$  value is obtained by applying electrochemical circuit fitting of the EIS plots. As shown in Figure 3D, the Randles

equivalent circuit was applied to fit the impedance data to determine the experimental values of the circuit elements. A low  $R_{ct}$  value is indicative of low electrode surface electron transfer resistance and thus greater electrode transducing capabilities or conductivity. The  $R_{ct}$  values for the PDMS@CNT/CNC, PDMS@CNT/CNC/PDMS@PANi and PDMS@CNT/CNC/PDMS@PANi@MIP patches were  $3573 \Omega$ ,  $2309 \Omega$ , and  $9382 \Omega$ , respectively. The conductivity of the PDMS@CNT/CNC provides evidence for good dispersion achieved between the PDMS insulating matrix and the CNC/CNT with the appropriate choice of the toluene and naphthalene solvent system, reported previously to preserve the excellent electrical property of CNTs.<sup>[21]</sup> The decrease in the observed  $R_{ct}$  value for the PDMS@CNT/CNC/PDMS@PANi signifies the faster electron kinetics impacted by the deposition of the highly conductive PANi layer to the PDMS@CNT/CNC surface. The PANi also increases the surface area for the electrode patch further enhancing the charge transfer kinetics. The enhanced conductivity can be attributed to the synergistic effect of the interpenetrating network bridging structures of PANi emeraldine salt domains to the CNT, thus inducing a charge transfer from PANi quinoid unit to

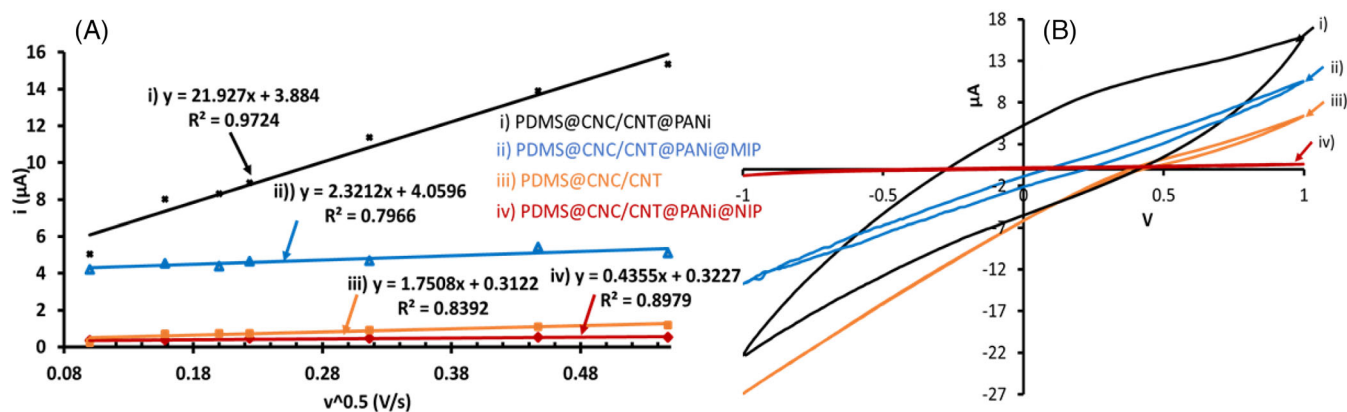


FIGURE 4 (A) Comparison of cathodic peak current as a function of square root of scan rates for 25 mM  $\text{K}_3\text{Fe}(\text{CN})_6$  in 0.1 M KCl CVs for different sensor patches; (B) Representative CVs at 0.1 V/s scan rate for different sensor patches

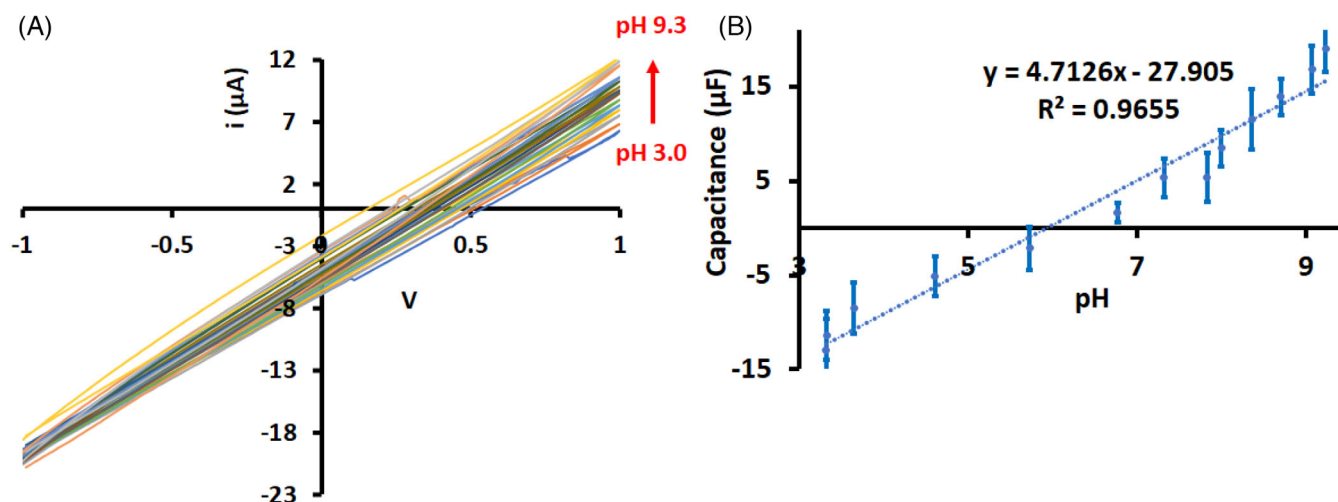


FIGURE 5 (A) Overlapped voltammograms for PDMS@CNT/CNC/PDMS@PANi pH sensor for different solutions of pH 3.0-9.3; (B) Resulting linear regression of capacitance as a function of pH for the PDMS@CNT/CNC/PDMS@PANi pH sensor

CNT.<sup>[32]</sup> The addition of the MIP layer, on the other hand, increased the  $R_{ct}$  due to the insulation properties of the non-conductive poly(GMA-EGDMA) coating.

The electroactive surface area of the different sensor patches was further characterized by running CV of the redox couple 25 mM  $\text{K}_3\text{Fe}(\text{CN})_6$  in 0.1 M KCl at different scan rates (0.01, 0.025, 0.04, 0.05, 0.1, 0.2, 0.3 V/s) and applying the Randles-Sevcik equation.<sup>[33]</sup> Figure 4 shows the resulting linear profiles for cathodic peak current as a function of the square root of scan rates for different sensor patches. Evidently, the electroactive response was highest for PDMS@CNC/CNT@PANi due to the increased synergy in conductivity between the CNT and the PANi. The PDMS@CNC/CNT@PANi@MIP had a higher response due to the increased porosity compared to the NIP form, confirmed previously in the SEM images (Figure 3B,C). The overlapped CVs in Figure 4B

similarly evidences the relative sensitivity response of the different patches. Using the Randles-Sevcik equation, the electroactive surface areas for the PDMS@CNC/CNT, PDMS@CNC/CNT@PANi, PDMS@CNC/CNT@PANi@MIP, and PDMS@CNC/CNT@PANi@NIP were calculated to be 0.010  $\text{mm}^2$ , 0.13  $\text{mm}^2$ , 0.013  $\text{mm}^2$ , and 0.0025  $\text{mm}^2$ , respectively.

### 3.2 | Testing of the pH sensor patch response

Following characterization, the PDMS@CNC/CNT@PANi sensor patch was evaluated for its response to pH. Figure 5A shows an overlapped voltammogram for the pH sensor's response to different pH solutions. Figure 5B shows the resulting linear calibration

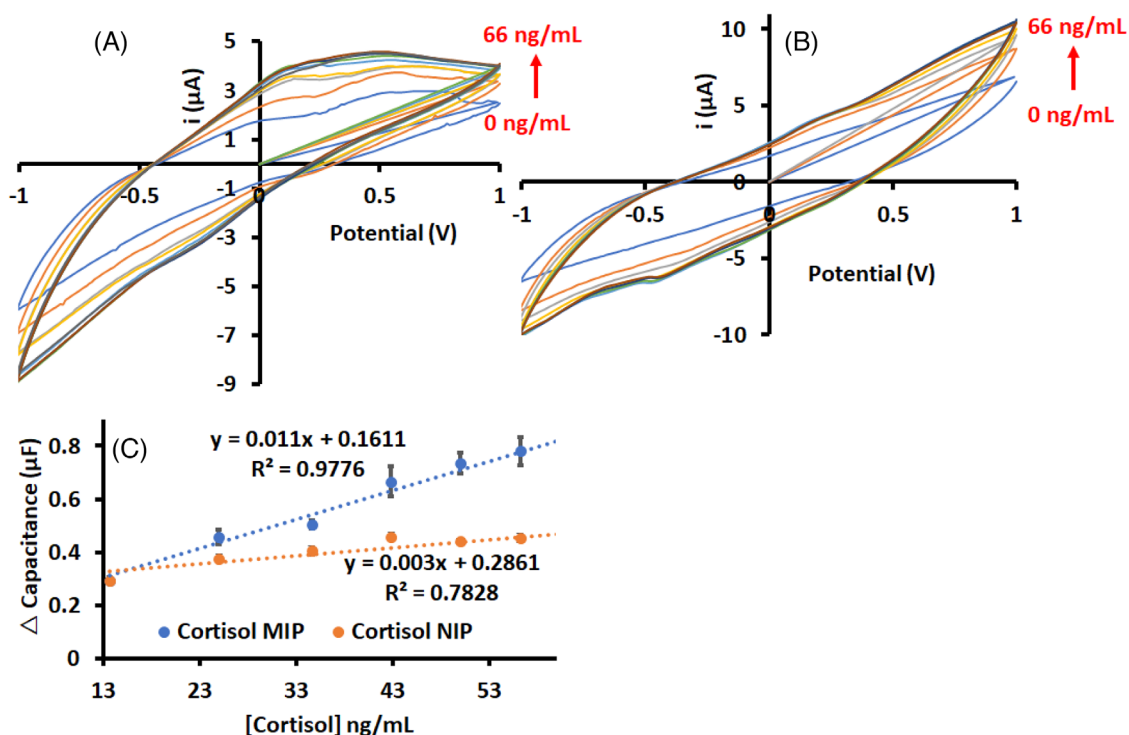


**FIGURE 6** Overlapped voltammograms for different cortisol standards (pH 7.1) for: (A) MIP sensor patch; (B) NIP sensor patch; (C) Resulting overlapped calibration plots of  $\mu\text{F}$  as a function of cortisol concentrations (pH 7.1) for the MIP and NIP sensor patches

( $R^2 = 0.96$ ), indicating a good response of the pH sensor within the pH range 3.0–9.3, with a calibration sensitivity of  $4.7 \mu\text{F}/\text{pH}$  at room temperature ( $23^\circ\text{C}$ ). The pH sensor was linearly responsive within the most relevant physiological range, as pH values lower than 3 and higher than 10 are rarely observed. The pH response mechanism of PANi based sensor depends on the transition from the emeraldine salt to the emeraldine base. The PDMS@CNT/CNC/PDMS@PANi pH sensor response was comparable to the Copper-Oxide/Polyaniline pH microelectrode array sensor fabricated using a rather involved microelectrical mechanical system technology recently reported by Wang et al.<sup>[34]</sup>

### 3.3 | Testing of the MIP/NIP cortisol sensor patch

The PDMS@CNT/CNC/PDMS@PANi@MIP and the NIP sensors were evaluated for the detection of cortisol at pH 4.5 and 7.1, a pH range that envelops the physiological pH flux in sweat. Figure 6A,B shows the overlapped voltammograms for different cortisol concentrations on a cortisol imprinted sensor patch and NIP patch, respectively. The voltammograms for the cortisol MIP sensor show two prominent peaks around 0.25 V and 0.50 V. However, these two peaks are significantly reduced in

the NIP sensor voltammograms. Figure 6c shows a comparison of the resulting calibration plots of  $\Delta$  capacitance as a function of cortisol concentration for both MIP (at both pH 7.1 and pH 4.5) and NIP cortisol sensor patches, the latter ran in cortisol solutions at pH 7.1. The difference of capacitance between the blank and the cortisol standards were averaged in the voltage range 0.25–0.50 V.

Evidently, the MIP cortisol sensor patch (pH 7.1) was more responsive to cortisol with a calibration sensitivity of  $0.011 \mu\text{F}/\text{ng}/\text{mL}$ , which is 366% higher than NIP sensor patch. The MIP cortisol sensor afforded a linear response ( $R^2 = 0.98$ ) to different cortisol concentrations from 0 to 66 ng/mL, compared to the significantly reduced linearity ( $R^2 = 0.78$ ) of the NIP patch. The increased response of the MIP sensor was expected, considering the cortisol selective cavities within the MIP network. The porous nature of the MIP compared to the polymer structure of the NIP is also evident in the SEM images in Figure 3B,C. This microporous surface morphology was further collaborated by the high electrochemical performance, evident by the high electron transfer shown in Figure 4A,B. As a control, the PDMS@CNT/CNC/PDMS@PANi without the poly(GMA-co-EGDMA) was tested and yielded a very low calibration sensitivity of  $0.0068 \mu\text{F}/\text{ng}/\text{mL}$  with poor linearity ( $R^2 = 0.77$ ), which supports the highly selective performance of the MIP as a cortisol receptor.

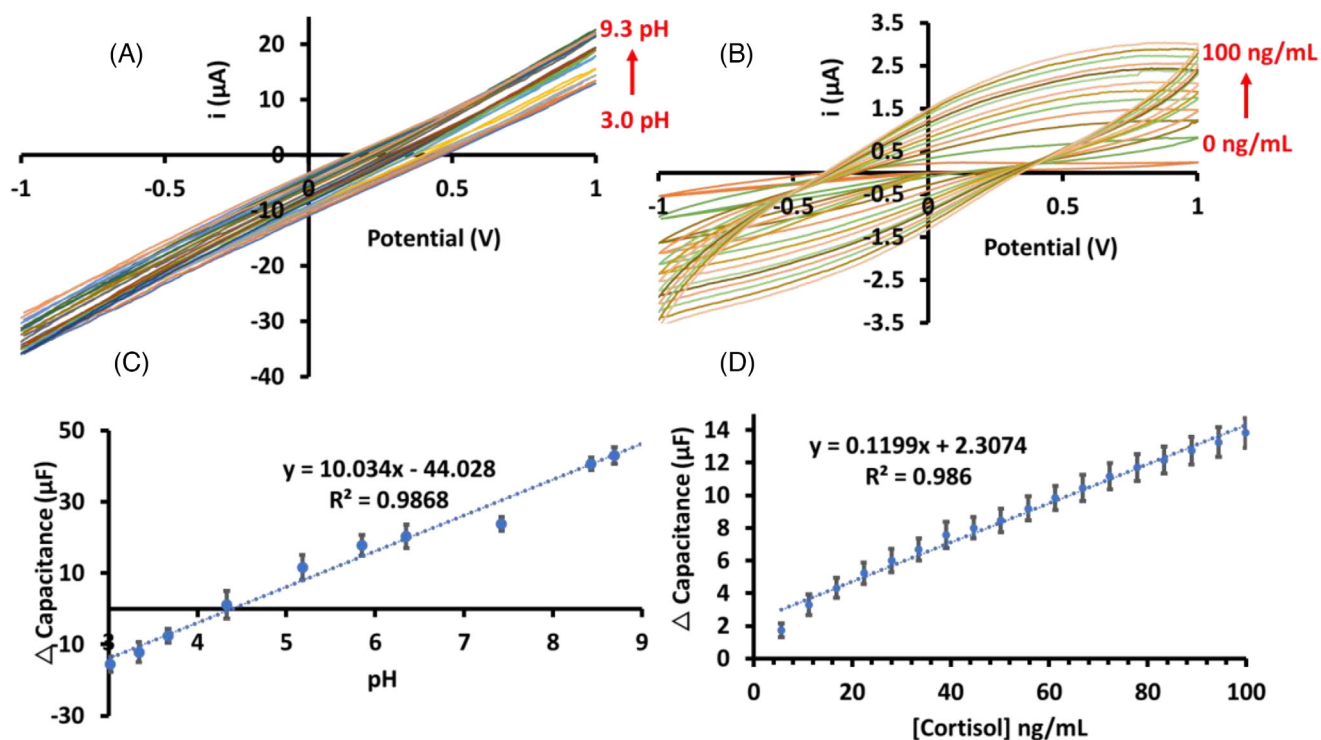


FIGURE 7 (A) Overlapped voltammograms of pH sensor in response to different pH solutions and variable cortisol concentrations; (B) Overlapped voltammograms of MIP sensor patch to different solutions of cortisol concentrations at variable pH; (C) Resulting overlapped calibrations plots for the pH sensor responding to different pH solutions and variable cortisol concentrations; (D) Resulting overlapped calibrations plots for the MIP sensor responding to different solutions of cortisol concentrations at variable pH

### 3.4 | The performance of the dual patch sensor for simultaneous detection of pH and cortisol

Biochemical markers that affect pH and cortisol co-exist within a sweat sample matrix. The detection of a suite of chemical markers simultaneously in a sensor array is an efficient approach to the prediction of wellbeing based on multiplex biomarker data. In our study, the pH and cortisol patches were printed on the same platform and used to detect pH and cortisol, both in a state of flux. The prototype of the dual pH and cortisol sensor array is shown in Figure 2B. The dual pH and cortisol sensor were immersed in 50 mL of an electrolyte (0.1 M HCl adjusted with 0.1 M NaOH) of pH of 3.0 and tested in a dynamic environment where both pH and cortisol concentration were increasing. Incremental volumes of 0.1 M NaOH and 1500 ng/mL cortisol standards were spiked onto the electrolyte solution, wherewith the dual sensor patch was immersed, followed by 1 min of stirring for equilibration, and subsequent detection by CV. Figure 7A,B shows the resulting overlapped voltammograms for the pH and the MIP cortisol sensor patches, respectively. Figure 7C,D shows the resulting calibration plots for the pH and cor-

tisol sensor patches, respectively. As shown in Figure 7C, even in the presence of cortisol, the pH sensor demonstrated excellent linearity ( $R^2 = 0.99$ ) in the pH range 3.0-9.3, with a calibration sensitivity of 10.0 and a limit of detection (LOD) of pH 2. Additionally, the cortisol MIP sensor patch responded linearly ( $R^2 = 0.99$ ) to increasing cortisol concentrations (0-100 ng/mL) even at variable pH, with a calibration sensitivity of  $0.12 \mu\text{F}/\text{ngmL}^{-1}$  cortisol. The LOD for the MIP cortisol sensor at variable pH was determined to be  $1.4 \pm 0.3 \text{ ng/mL}$ , well below the lower limit of the physiological cortisol sweat levels reported by several researchers.<sup>[25,35,36]</sup> The LOD was calculated as three times the standard deviation of the blank divided by the calibration slope.

To develop a more robust calibration, statistical analysis was applied to identify the voltages that best predict pH and cortisol concentration by developing a correlation response matrix between current and variable voltages. As shown in Figure S1, a model ( $\text{pH} = 1.11V_{0.26} + 8.34$ ) was developed based on the single best voltage predictor for pH correlation, resulting in an  $R^2$  of 0.990 and a holdout test RMSE of 0.32. For the cortisol sensor data, as shown in Figure S2, a model ( $\text{cortisol} = 94.2V_{0.48} + 22.8$ ) was developed based on the single best voltage predictor for cortisol

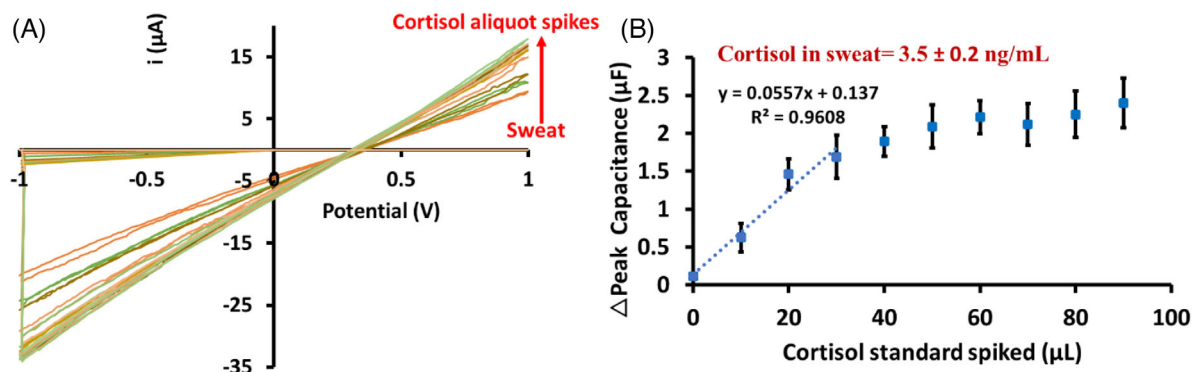


FIGURE 8 (A) Overlapped voltammograms of cortisol sensor patch in response to 0.1 M KCl, real sweat, and 10  $\mu\text{L}$  sequential addition of 1500 ng/mL cortisol standard; (B) Resulting standard addition calibration plot for the cortisol sensor patch

correlation, resulting in an  $R^2$  of 0.991 and a holdout test RMSE of 4.27.

### 3.5 | Real sweat analysis

The dual pH and cortisol sensors were tested for detection using real human sweat. A 1000  $\mu\text{L}$  0.1 M KCl blank solution was deposited on the dual sensors and analyzed by CV. Then, a 50  $\mu\text{L}$  of sweat sample aliquot from a volunteer was deposited to the blank aliquot and analyzed, followed by a 10  $\mu\text{L}$  sequential addition of 1500 ng/mL of cortisol standard. Figure 8A shows the overlapped voltammograms obtained from blank, sweat, and the cortisol standard additions. The resulting standard addition calibration from cortisol MIP sensor response is shown in Figure 8B, with the capacitance signal response averaged between 0.25 and 0.50 V. Based on this standard addition calibration, the cortisol concentration in the sweat was determined to be  $3.5 \pm 0.2$  ng/mL that is within the acceptable physiological range.<sup>[25,35,36]</sup> Following the sweat addition, the pH sensor chamber recorded a capacitance of 21.60  $\mu\text{F}$ , which corresponded to a pH of  $6.5 \pm 0.1$ , based on the external standard calibration curve in Figure 7C. This value is within the acceptable physiological range of sweat (pH 4.5-7).<sup>[5]</sup> The pH sensor patch results for real sweat were also within 2% of the value obtained using the commercial pH electrode.

### 3.6 | Evaluation of the dual pH and cortisol MIP sensor in wearable operation mode

The dual microneedle sensor was also tested as a wearable device for the detection of pH and cortisol in sweat. The microneedle sensor patches were attached to the surface of the skin on the upper arm and secured using a tape as shown in Figure 9A. Figure 9B and 9C, respectively,

show a comparison of the voltammograms for the pH and cortisol sensor response to 0.1 M KCl compared to human sweat, following 30 mins of vigorous exercise. As shown in Figure 9b, the rapid response of the PANi sensor layer to change in pH following exposure to sweat is evident as indicated by the rapid change in current of the cyclic voltammograms when compared to that of 0.1 M KCl. Sweat is a complex biological matrix and the capacitance of the PANi sensor layer could further be influenced by these matrices. However, the accuracy of the pH sensor is not in question. Using the external calibration methods in Figure 7C and 7D, the pH and cortisol were determined to be  $6.3 \pm 0.1$  and  $3.4 \pm 0.2$  ng/mL, respectively, which closely matches the results obtained from standard addition calibrations. Future studies will explore the depth of penetration and evaluate whether the sensor is sampling the interstitial fluid or just sweat. We submit the data collected in our case would be a combination of sweat and possibly interstitial fluid.

### 3.7 | Robustness and reusability of the pH and cortisol MIP sensor

To evaluate the patch sensors, the cortisol MIP sensor was evaluated for stability with usage and storage. A 0.1 M KCl blank and a 20 ng/mL cortisol standard were analyzed by the same sensor once every 2 days (with each analysis done in triplicate) over 30 days while stored at room temperature conditions. Three MIP sensors were tested. Following each use, the MIP sensor was electrochemically cleaned using 0.1 M KCl described in the methods section. Based on this study, the sensor's stability and reusability over an extended period of use is evident, as shown in the overlapped voltammograms in Figure 10A, resulting from the cortisol detection and cleaning cycles over 30 days. A representative capacitance data for the cortisol standard and blank measurement is shown in Figure 10B. Evidently, the

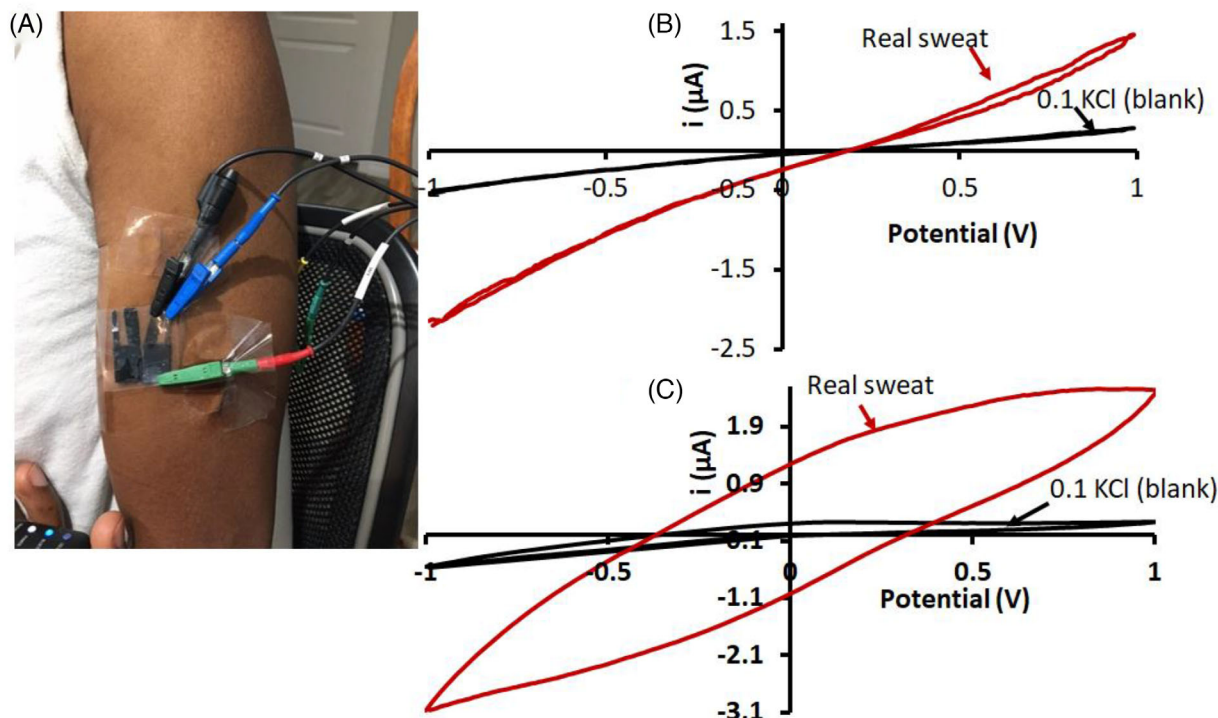


**FIGURE 9** (A) Photograph of the dual pH and cortisol sensor in wearable mode; (B) Overlapped voltammogram showing the pH sensor chamber response to 0.1 M KCl compared to human sweat; (C) Overlapped voltammogram showing the cortisol sensor chamber response to 0.1 M KCl compared to human sweat

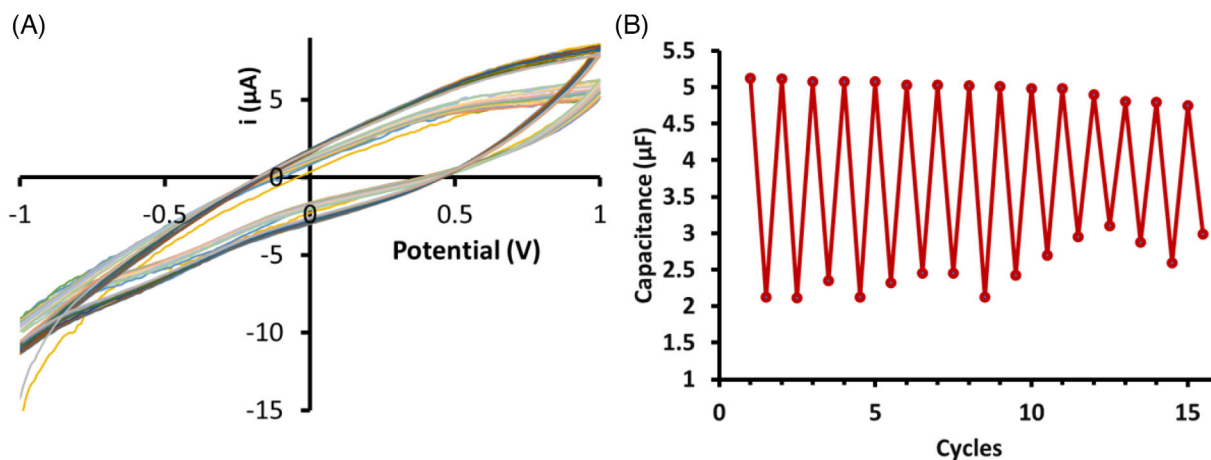


**FIGURE 10** (A) Overlapped voltammograms of MIP sensor patch following 15 wash and use cycles, detecting 0.1 M KCl and 20 ng/mL cortisol standards over 30-day period; (B) Summary of the capacitance data of 0.1 M KCl and 20 ng/mL cortisol standard after 15 cycles of analysis over a 30-day period

capacitance barely changed over the 30 days of storage, usage, electrochemical cleaning cycling. Further, based on the three different sensors' data, the intra-batch percent relative standard deviation (%RSD) was determined to be 2.4%. The inter-batch precision (%RSD for three different sensors) was determined to be 4.7%.

#### 4 | CONCLUSION

Both pH and cortisol levels are insightful biochemical markers for indexing physiological stress and general wellbeing. This manuscript demonstrates an inexpensive wearable sensor platform for dual detection of pH and

cortisol in sweat. Comprising a flexible conductive PDMS patch as the substrate and utilizing the pH responsibility of PANi and cortisol poly (GMA-co-EGDMA) MIP, the dual electrochemical sensor affords accurate simultaneous detection of pH and cortisol, respectively. With a rapid response of 1 min, the pH sensing chamber responded linearly to pH in the 3.0-9.3 range, while the cortisol sensor was linear between 0 and 100 ng/mL with a LOD of  $1.4 \pm 0.3$  ng/mL evaluated at variable pH of 3.0-9.3. The stability and reusability of the sensors were verified by testing the sensor's response to cortisol over 15 detection cycles performed over a 30-day period, yielding a %RSD of 2.4%. The practical usability of the dual pH and cortisol sensors has been confirmed with their accurate application for in-situ and ex-situ monitoring of real human sweat samples.

### ACKNOWLEDGMENTS

Mugo research group acknowledges funding from Natural Sciences and Engineering Research Council of Canada (NSERC).

### CONFLICT OF INTEREST

The authors declare no conflict of interest.

### COMPLIANCE WITH ETHICAL STANDARDS

Informed consent was obtained from the student volunteer participant included in the study. The study was approved by the MacEwan Research Ethics Board (REB) to ascertain the study was performed in accordance with acceptable ethical standards.

### DATA AVAILABILITY STATEMENT

Not Applicable

### REFERENCES

1. A. J. Bandodkar, I. Jeeran, J. Wang, *ACS Sens.* **2016**, *1*, 464–482. <https://doi.org/10.1021/acssensors.6b00250>.
2. S. Roy, M. David-Pur, Y. Hanein, *ACS Appl. Mater. Interfaces.* **2017**, *9*, 35169–35177. <https://doi.org/10.1021/acsami.7b07346>.
3. S. Jadoon, S. Karim, M. R. Akram, A. Kalsoom Khan, M. A. Zia, A. R. Siddiqi, G. Murtaza, *Int. J. Anal. Chem.* **2015**, *2015*, 1–7. <https://doi.org/10.1155/2015/164974>.
4. Y. H. Caplan, B. A. Goldberger, *Anal. Toxicol.* **2001**, *25*, 396–399. <https://doi.org/10.1093/jat/25.5.396>.
5. W. Dang, L. Manjakkal, W. T. Navaraj, L. Lorenzelli, V. Vinciguerra, R. Dahiya, *Biosens. Bioelectron.* **2018**, *107*, 192–202. <https://doi.org/10.1016/j.bios.2018.02.025>.
6. J. Bijman, P. M. Quinton, *Pediatr. Res.* **1987**, *21*, 79–82. <https://doi.org/10.1203/00006450-198701000-00017>.
7. M. J. Patterson, S. D. R. Galloway, M. A. Nimmo, *Exp. Physiol.* **2000**, *85*, 869–875. <https://doi.org/10.1111/j.1469-445X.2000.02058.x>.
8. S.H. Kuo, C.J. Shen, C.F. Shen, C.M. Cheng, *Diagnostics.* **2020**, *10*, 107. <https://doi.org/10.3390/diagnostics10020107>.
9. S. M. Mugo, J. Alberkant, *Anal. Bioanal. Chem.* **2020**, *412*, 1825–1833. <https://doi.org/10.1007/s00216-020-02430-0>.
10. R. C. Kessler, P. Berglund, O. Demler, R. Jin, K. R. Merikangas, E. E. Walters, *Arch. Gen. Psychiatry.* **2005**, *62*, 593. <https://doi.org/10.1001/archpsyc.62.6.593>.
11. S. K. Putnam, C. Lopata, M. L. Thomeer, M. A. Volker, J. D. Rodgers, *J. Dev. Phys. Disabil.* **2015**, *27* 453–465. <https://doi.org/10.1007/s10882-015-9428-2>.
12. G. de Vaan, R. Beijers, M. P. J. Vervloed, H. Knoors, K. A. Bloeming-Wolbrink, C. de Weerth, L. Verhoeven, *Front. Educ.* **2020**, *5*, 540387. <https://doi.org/10.3389/educ.2020.540387>.
13. C. W. Schupp, D. Simon, B. A. Corbett, *J. Autism Dev. Disord.* **2013**, *43*, 2405–2417. <https://doi.org/10.1007/s10803-013-1790-2>.
14. O. Parlak, S. T. Keene, A. Marais, V. F. Curto, A. Salleo, *Sci. Adv.* **2018**, *4*, eaar2904. <https://doi.org/10.1126/sciadv.aar2904>.
15. E. G. Spratt, J. S. Nicholas, K. T. Brady, L. A. Carpenter, C. R. Hatcher, K. A. Meekins, R. W. Furlanetto, J. M. Charles, *J. Autism Dev. Disord.* **2012**, *42*, 75–81. <https://doi.org/10.1007/s10803-011-1214-0>.
16. B. A. Corbett, C. W. Schupp, S. Levine, S. Mendoza, *Autism Res.* **2009**, *2*, 39–49. <https://doi.org/10.1002/aur.64>.
17. J. R. Sempionatto, I. Jeeran, S. Krishnan, J. Wang, *Anal. Chem.* **2020**, *92*, 378–396. <https://doi.org/10.1021/acs.analchem.9b04668>.
18. K. Takeuchi, N. Takama, B. Kim, K. Sharma, P. Ruther, O. Paul, *2018 IEEE CPMT Symposium Japan (ICJSJ)*, IEEE, Kyoto, **2018**, 85–88. <https://doi.org/10.1109/ICJSJ.2018.8602945>.
19. K. Takeuchi, N. Takama, R. Kinoshita, T. Okitsu, B. Kim, *Biomed. Microdevices.* **2020**, *22*, 79. <https://doi.org/10.1007/s10544-020-00532-1>.
20. P. P. Samant, M. M. Niedzwiecki, N. Raviele, V. Tran, J. Mena-Lapaix, D. I. Walker, E. I. Felner, D. P. Jones, G. W. Miller, M. R. Prausnitz, *Sci. Transl. Med.* **2020**, *12*, eaaw0285. <https://doi.org/10.1126/scitranslmed.aaw0285>.
21. T. Mulembo, G. Nagai, H. Tamagawa, T. Nitta, M. Sasaki, *J. Appl. Polym. Sci.* **2019**, *136*, 48167. <https://doi.org/10.1002/app.48167>.
22. J. Kim, J. R. Sempionatto, S. Imani, M. C. Hartel, A. Barfidokht, G. Tang, A. S. Campbell, P. P. Mercier, J. Wang, *Adv. Sci.* **2018**, *5*, 1800880. <https://doi.org/10.1002/advs.201800880>.
23. H. J. Park, J. H. Yoon, K. G. Lee, B. G. Choi, *Nano Convergence.* **2019**, *6*, 9. <https://doi.org/10.1186/s40580-019-0179-0>.
24. M. Kaempgen, S. Roth, *J. Electroanal. Chem.* **2006**, *586*, 72–76. <https://doi.org/10.1016/j.jelechem.2005.09.009>.
25. M. Jia, W. M. Chew, Y. Feinstein, P. Skeath, E. M. Sternberg, *Analyst* **2016**, *141*, 2053–2060. <https://doi.org/10.1039/C5AN02387D>.
26. J. A. Martin, J. L. Chávez, Y. Chushak, R. R. Chapleau, J. Hagen, N. Kelley-Loughnane, *Anal. Bioanal. Chem.* **2014**, *406*, 4637–4647. <https://doi.org/10.1007/s00216-014-7883-8>.
27. O. Ramström, L. Ye, K. Mosbach, *Chem. Biol.* **1996**, *3*, 471–477. [https://doi.org/10.1016/S1074-5521\(96\)90095-2](https://doi.org/10.1016/S1074-5521(96)90095-2).
28. A. Groza, A. Surmeian, *J. Nanomater.* **2015**, *2015*, 1–8. <https://doi.org/10.1155/2015/204296>.
29. V. Hospodarova, E. Singovszka, N. Stevulova, *AJAC.* **2018**, *09*, 303–310. <https://doi.org/10.4236/ajac.2018.96023>.
30. M. Trchová, J. Stejskal, *Pure Appl. Chem.* **2011**, *83*, 1803–1817. <https://doi.org/10.1351/PAC-REP-10-02-01>.
31. I. S. Stefanović, B. M. Ekmešćić, D. D. Maksin, A. B. Nastasović, Z. P. Miladinović, Z. M. Vuković, D. M. Micić, M. V. Pergal, *Ind.*

- Eng. Chem. Res.* **2015**, *54*, 6902–6911. <https://doi.org/10.1021/acs.iecr.5b01285>.
32. Dhanjai, S. M. Mugo, W. Lu, *Anal. Bioanal. Chem.* **2020**, *412*, 7063–7072. <https://doi.org/10.1007/s00216-020-02836-w>.
33. B. Habibi, M. Jahanbakhshi, *Sens. Actuators B Chem.* **2014**, *203*, 919–925. <https://doi.org/10.1016/j.snb.2014.06.096>.
34. X. Wang, L. Sun, T. Wang, Y. Shi, *IEEE Sensors J.* **2020**, *20*, 14598–14606. <https://doi.org/10.1109/JSEN.2020.3010709>.
35. E. Russell, G. Koren, M. Rieder, S. H. M. Van Uum, *Ther. Drug Monit.* 30–34, **2013**, 36. <https://doi.org/10.1097/FTD.0b013e31829daa0a>.
36. R. M. Torrente-Rodríguez, J. Tu, Y. Yang, J. Min, M. Wang, Y. Song, Y. Yu, C. Xu, C. Ye, W. W. IsHak, W. Gao, *Matter* **2020**, *2*, 921–937. <https://doi.org/10.1016/j.matt.2020.01.021>.

## SUPPORTING INFORMATION

Additional supporting information may be found online in the Supporting Information section at the end of the article.

**How to cite this article:** S. M. Mugo, W. Lu, M. Wood, S. Lemieux *Electrochem Sci Adv.* 2021, e2100039. <https://doi.org/10.1002/elsa.202100039>